Gesch *et al. J. Mater. Inf.* **2025**, *5*, 42
DOI: 10.20517/jmi.2025.23

Journal of Materials Informatics

Research Article

Open Access

Check for updates

Accelerating phase-field simulation of coupled microstructural evolution using autoencoder-based recurrent neural networks

Aidan Gesch, Chongze Hu*

Department of Aerospace Engineering and Mechanics, The University of Alabama, Tuscaloosa, AL 35487, USA.

***Correspondence to:** Prof. Chongze Hu, Department of Aerospace Engineering and Mechanics, The University of Alabama, 251 Shelby Ln, Tuscaloosa, AL 35487, USA. E-mail: hucz@ua.edu

How to cite this article: Gesch, A.; Hu, C. Accelerating phase-field simulation of coupled microstructural evolution using autoencoder-based recurrent neural networks. *J. Mater. Inf.* **2025**, *5*, 42. https://dx.doi.org/10.20517/jmi.2025.23

Received: 7 Apr 2025 **First Decision:** 7 May 2025 **Revised:** 20 May 2025 **Accepted:** 26 May 2025 **Published:** 25 Jun 2025

Academic Editors: Ming Hu, Xiang-Dong Ding **Copy Editor:** Pei-Yun Wang **Production Editor:** Pei-Yun Wang

Abstract

Accelerated phase-field frameworks leveraging time-dependent neural networks have recently been developed to accelerate microstructure-based phase-field simulations in both temporal and spatial domains. However, most of these frameworks have been designed for phase-field problems involving a single variable field, such as spinodal decomposition. In this study, we developed an accelerated framework for predicting the microstructural evolution of Ostwald ripening, a classical phase-field problem involving multiple interdependent parameter fields. This framework integrates various components: high-throughput phase-field simulations for generating high-quality microstructure database, autoencoder-based dimensionality reduction to transform 2D microstructure images into latent representations, and long short-term memory (LSTM) networks serving as the microstructure learning engine. Our results demonstrate that autoencoder techniques can effectively reduce the large dimension of microstructure images into 16 key values, while maintaining high accuracy in reconstructing these reduced representations back to their original space. Using these latent representations, LSTM models are employed to capture the key microstructural features of Ostwald ripening and predict their evolution over future time sequences, with a speedup of approximately 3.35×10^5 times compared to the high-fidelity phase-field simulations. The accelerated framework presented in this work is the first data-driven emulation specifically designed for coupled phase-field problems, and it can be easily extended to predict other evolutionary phenomena with more complex microstructural features.

Keywords: Accelerated phase-field framework, microstructural evolution, recurrent neural networks, dimensionality reduction, Ostwald ripening

INTRODUCTION

Phase-field simulation is a highly powerful computational tool for modeling the dynamic behaviors of microstructures across a wide range of material systems[1-4]. It employs a variety of approaches, from continuum theory to classical thermodynamics, to explore the evolution of material interfaces in both spatial and temporal resolutions. Unlike atomistic simulations, such as molecular dynamics and first-principles, phase-field simulations do not rely on atomistic details of the materials, enabling them to study materials dynamics over large length and time scales. For instance, these simulations are always used to model the microstructural evolutions of materials in various scenarios such as spinodal decomposition[5,6], Ostwald ripening[7], grain growth[8-10], and dendrite growth[11-13]. Additionally, phase-field simulations have been broadly applied to practical engineering problems in solid mechanics[14-16], fluid mechanics[17-19], fracture mechanics[20-22], and other disciplines[23-25].

A major drawback of high-fidelity phase-field simulations is their high computational cost, which stems from the need to solve a system of partial differential equations (PDEs) for various continuous variables that evolve both in space and in time[1]. In addition, phase-field simulations typically require refined spatio-temporal discretization and an accurate description of the free energy of the entire system, making them cumbersome to implement for a specific engineering application. To effectively solve the convoluted PDEs, direct numerical solvers, such as finite-elements[26-28], finite-difference[29-31], finite-volume[32], and spectral methods[33-35], are widely adopted for phase-field simulations. Despite their improved effectiveness, these numerical schemes still require a large number of degrees of freedom and substantial computational resources to obtain accurate spatial and temporal solutions[33,36,37]. This limits the performance of phase-field simulation, particularly when dealing with large or complex problems. One approach to accelerate the solution of PDEs is to leverage the high-performance computing (HPC) architectures. For instance, researchers have found that graphics processing unit (GPU)-based algorithm can speed up phase-field simulation by 50 times compared to central processing unit (CPU) implementations[38]. Yet, the high demand and long waiting times for HPC resources may limit their effectiveness in speeding up phase-field simulations. As a result, developing alternative strategies to accelerate phase-field simulations has become an urgent research task.

As an emerging alternative, machine learning techniques are rapidly gaining research interest in the phase-field communities due to their universal function approximation capabilities[39]. For instance, deep neural networks (DNNs) have been adopted to learn the high-dimensional free energy functions and their derivatives from atomistic simulations to solve PDEs for phase-field simulations[40-42]. Data-driven surrogate models, which use a reduced-order statistical representation of the microstructures combined with regression models to link phase-field input parameters (e.g., deposition rate and phase fraction), have been employed to forecast the corresponding microstructure at a given time[43,44]. Although these examples illustrate the huge potential to enhance the usability of integrating machine-learning models into phase-field simulations, such integration must be systematically examined to ensure high credibility. For instance, the accuracy and robustness of these integrated machine-learning models highly rely on the quality of the microstructure database used to train them. Generating these databases is both costly and often challenging to achieve, especially for real-world engineering problems.

Another strategy involves developing an artificial microstructure-learning engine to accelerate the prediction of microstructural evolution into the unknown future time sequence. Based on the architecture of these learning engines, two major types of accelerated phase-field frameworks have been developed to date: latent dynamics models (LDMs) and pixel-space dynamics models (PSDMs)[39]. LDMs typically learn microstructures in the latent space using dimensionality reduction techniques, and then employ history-

dependent machine learning models, such as recurrent neural networks (RNNs), to predict the evolution of microstructures in future time sequence[45-50]. PSMDs directly approximate the microstructural dynamics from their original two-dimensional (2D) or three-dimensional (3D) space using the physics-informed neural networks, such as neural operator learning. These PSDMs generally incorporate a temporal-conditioning mechanism, which can further improve the accuracy and efficiency of time-to-solution predictions for microstructural evolution. For instance, a deep-learning-based neural network with a U-Net architecture has been developed to predict the microstructural evolution for a range of phase-field problems, including spinodal decomposition, dendrite growth, and thin film deposition[51]. Despite their outstanding performance, most existing accelerated frameworks, including both LDMs and PSDMs have been developed for relatively simple phase-field problems with a single evolution field, such as spinodal decomposition[45-49]. Accelerated frameworks for more complex, coupled microstructural evolution problems are still scarcely developed, thereby motivating this study.

Using the classical benchmark problem Ostwald ripening as a modeling system[52], we in this work developed a highly integrated framework to accelerate the microstructural evolution of coupled phase fields. This accelerated framework integrates high-throughput phase-field modeling, dimensionality reduction, and long short-term memory (LSTM) networks to predict the microstructural evolution of Ostwald ripening in latent representations. Specifically, autoencoders are first used to transform the 2D microstructure images into a low-dimensional space for training LSTM models. Once trained, the LSTM models are employed to predict the temporal evolution of microstructures in the latent space, and then the autoencoder is used to reconstruct these predicted microstructure sequences back into the original 2D space. Finally, supervised learning techniques are applied to predict the correlations between coupled fields within the latent space, thereby further enhancing the overall efficiency of this accelerated phase-field framework.

MATERIALS AND METHODS

Figure 1 illustrates a simplified workflow of our accelerated framework for Ostwald ripening[52]. The high-throughput phase-field simulations are first performed with various input parameters to generate a large database of microstructural evolution over time [Figure 1A]. Using the large number of microstructure images, we employ an autoencoder-based dimensionality reduction technique to reduce the data to the low-dimensional space. Specifically, each parameter field in Ostwald ripening can be defined by a continuous function $X(\mathbf{x}, t)$, where $\mathbf{x}$ and t represent a 2D spatial domain and time, respectively. After dimensionality reduction, the microstructure of each parameter field can be given by a multivariate time-series $\mathbf{x} = (\mathbf{x}_1, \mathbf{x}_2, ..., \mathbf{x}_N)$, where x_i is a vector in latent space and represents the reduced microstructure at time $t = t_i$ [Figure 1B]. Next, we use one of the most popular RNN models, LSTM, to learn the nature of microstructure evolution of Ostwald ripening in the latent space [Figure 1C]. This is realized by establishing a functional relationship among the low-dimensional representation x_i, the current time step t_i and prior lagged values (t_{i-1}, t_{i-n}).

$$x_i = f(x_{i-1}, ..., x_{i-n}) \tag{1}$$

The LSTM-based microstructure-learning engine can efficiently learn the microstructural evolution as a function of any model input and predict future time frames without the need to perform computationally expensive phase-field simulations. Finally, the autoencoder will be used to transform the LSTM-predicted microstructure in latent space back to full-scale 2D images [Figure 1D].

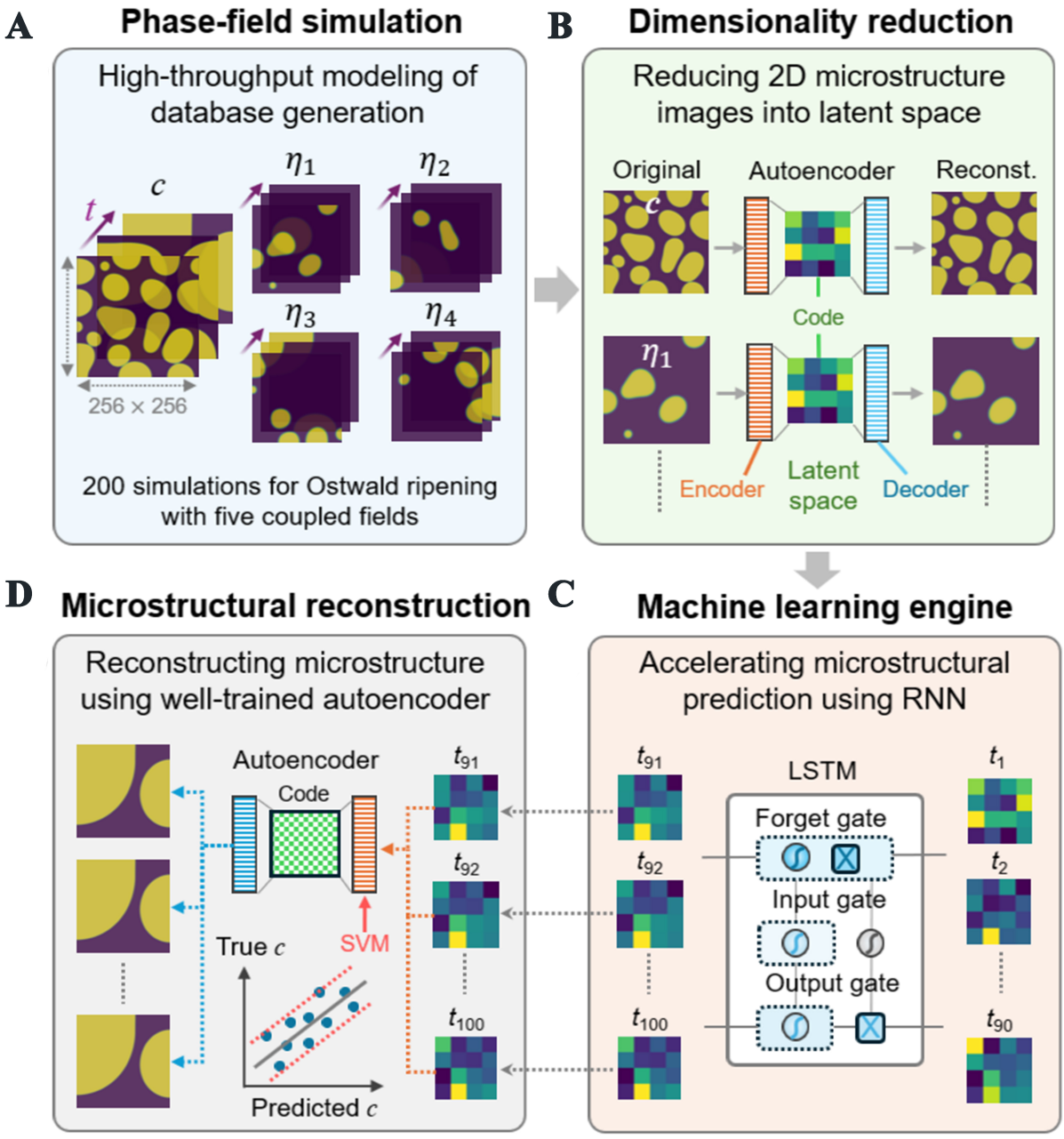

Figure 1. Workflow of accelerated phase-field framework for Ostwald ripening problem. (A) High-throughput phase-field simulations of generating database of 2D microstructure images for five coupled fields in Ostwald ripening; (B) Dimensionality reduction of 2D microstructural images into latent space using autoencoder; (C) LSTM-based machine learning engine to accelerate the microstructure prediction in latent space; (D) Reconstruction of latent microstructures back to original 2D space using well-trained autoencoder models, along with machine-learning prediction of feature correlation between the coupled phase fields. 2D: Two-dimensional; LSTM: long short-term memory.

Phase-field model of the Ostwald ripening

The phase-field modeling of Ostwald ripening involves a system consisting of both ordered and disordered phases. The solute concentration, c (x, t), is a conservative field that describes the atomic fraction of solute diffusion within a matrix. The structural order parameter, η, is a non-conservative field that describes different phases based on order parameters, such that $\eta = 0$ represents α phase and $\eta = 1$ means β phase. The

free energy landscape of the system can be expressed by[52]:

$$F = \int \left(f_{chem}(c, \eta_1, \eta_2, ..., \eta_p) + \frac{\kappa_c}{2}|\nabla c|^2 + \sum_{i=1}^{p} \frac{\kappa_\eta}{2}|\nabla \eta_p|^2 \right) dV \quad (2)$$

where f_{chem} is chemical free energy density, κ_c is gradient energy coefficient for solute field, κ_η is the gradient energy coefficients for structural order parameters η_p, and p is the number of structural order parameters. We set $p = 4$ because it is a commonly used value used in nickel-based superalloys[52]. The f_{chem} is determined by:

$$f_{chem}(c, \eta_1, \eta_2, ..., \eta_p) = f^\alpha(c)[(1 - h(\eta_1, \eta_2, ..., \eta_p)] + f^\beta(c)[(h(\eta_1, \eta_2, ..., \eta_p)] + wg(\eta_1, \eta_2, ..., \eta_p) \quad (3)$$

where f^α and f^β are the chemical free energy density of the α and β phases, h (η_1, η_2, ..., η_p) is an interpolation function, g (η_1, η_2, ..., η_p) is a double-well function, and w is a parameter which controls the height of the double-well barrier. The mathematical formulations and more detailed explanations for f^α, f^β, h, and g can be found in prior study[52]. Since c (**x**, t) must obey contiuity equation, the evolution of c is governed by Cahn-Hilliard equation[5], which is derived from an Onsager force-flux relationships[53]:

$$\frac{\partial c}{\partial t} = \nabla \cdot \left[M \nabla \left(\frac{\partial f_{chem}}{\partial c} - \kappa_c \nabla^2 c \right) \right] \quad (4)$$

where M is the mobility of solute. The evolution of η_p is governed by Allen-Cahn equation[54] based on gradient flow:

$$\frac{\partial \eta_p}{\partial t} = -L \left[\frac{\partial f_{chem}}{\partial \eta_p} - \kappa_{\eta_p} (\nabla^2 \eta_p) \right] \quad (5)$$

where L is the kinetic coefficient associated with the structural order parameter η_p. By considering one solute field and four structural order parameter fields, the Ostwald ripening problem in this study can be treated as a five-phase coupled phase-field problem.

Database generation via high-throughput phase-field simulations

All phase-field simulations for Ostwald ripening were performed using the Mesoscale Mutli-Physics Phase-Field Simulator (MEMPHIS) code[55,56]. By analyzing the distribution of input parameters and their corresponding microstructures, we found that the most influential input parameters for generating diverse microstructural features are solute mobility (M), ranging from 4.5 to 5, the equilibrium phase fraction (c_α), ranging from 0.15 to 0.45, the initial composition average (c_0), ranging from 0.45 to 0.55, and the initial composition variance (ϵ), ranging from 0.04 to 0.08, as shown in Supplementary Figure 1.

For these dominant input parameters, we randomly sample these parameters in their optimal ranges to ensure they can capture a diverse set of microstructure images. Supplementary Figure 1 shows that 200 phase-field simulations with varying input parameters can effectively sample the entire parameter space, ensuring that our microstructure database is sufficiently comprehensive to capture the key features of coupled parameter fields across the spatial domain for this Ostwald ripening problem. Other parameters necessary for the simulation are adopted as constants, and they are: $\kappa_c = \kappa_\eta = 3$, $\rho = \sqrt{2}$, $w = 1$, $\alpha = 5$, and $L = 5$[52].

Each phase-field simulation was performed on a 2D square grid with a uniform mesh composed of 256 × 256 grid points. We used dimensionless spatial and temporal discretization parameters, with a spatial discretization of $\Delta x = \Delta y = 1$, and a temporal discretization of $\Delta t = 1 \times 10^{-3}$. For each simulation, the total of

time steps is set to 30,000,000, and no-flux boundary conditions are applied to all sides of the domain, ensuring that microstructures stick to the edges of the simulation box and do not pass through. All microstructure evolutionary trajectories are evenly divided into the 100 intervals, ensuring that each simulation has a 256 × 256 × 100 data points. As it does not have microstructures, it is not included in the dataset, but a snapshot of the initial condition is also saved for each trajectory. Given the five coupled fields in each simulation, the total size of a microstructure evolution for 200 simulations is 256 × 256 × 100 × 5 × 200 (26 billion data points) generated in this work. Each phase-field simulation takes about 377 minutes by using 16 CPUs on HPC facilities at the Alabama Supercomputer Center to predict the microstructure evolution of Ostwald ripening over the 100 time frames. All microstructure databases have been uploaded to the materials data facility (MDF)[57,58] and the database is already available online[59].

Dimensionality reduction of microstructural evolution

A key component of our accelerated framework is the manifold hypothesis, which suggests that high-dimensional data lies near a low-dimensional manifold inside high-dimensional space[60]. Similarly, many studies have shown that high-dimensional microstructure images can be effectively transformed into a lower-dimensional space while preserving key features to represent their evolutionary behaviors. Therefore, we applied dimensionality reduction to transform the 2D microstructure images of Ostwald ripening into a reduced space. A recent study by Desai *et al.* has demonstrated that the autoencoder is a very powerful technique in transforming microstructure images into low-dimensional space and provides smooth trajectories in the latent space[61]. As such, we primarily adopted this approach to process the 2D images of Ostwald ripening for all five coupled fields [Figure 1B].

Autoencoder

An autoencoder is an unsupervised learning technique that is designed to encode high-dimensional data into a compressed and meaningful representation[62,63]. Briefly speaking, an autoencoder has two major components: an encoder that maps the input data into a lower-dimensional space, and a decoder that reconstructs the original data from this compressed representation [Figure 1B]. The code typically has a space Z, which is smaller than the original space of input data but can still retain useful features in its compressed space. This capability makes autoencoders a powerful tool for transforming 2D microstructure image data, X ($\mathbf{x}$, t), into a low-dimensional representation, Z (x_i, t)[64,65]. The microstructure dataset used to train the autoencoders consists of 80,000 2D images, which is 80% of all microstructure images generated for Ostwald ripening. The microstructure images from the early time frames (1 to 80) were preferentially selected as training data due to their larger diversity, while those from later time frames tend to exhibit more uniform and constant features because most of the systems have reached a fully stabilized state after time frame 80 and were thus included less often. This selection strategy also ensured that each microstructure trajectory has an equal number of microstructure images (80) included in the entire dataset. The training routine further creates a split between training data and validation data, with 80% used for training and 20% used for testing. The autoencoders were trained to minimize the reconstruction error using the binary cross-entropy (BCE) as the loss function[66]. We selected BCE as the performance metric for evaluating the reconstruction performance of the autoencoder due to two main reasons: (i) its focus on the probabilistic difference between the predicted and actual outputs when there are discrete options, such as in phase selection during reconstruction; and (ii) faster convergence speed during the training process. The training was conducted for a total of 1,400 epochs, and the autoencoder reached convergence after approximately 700 epochs, based on the training and validation loss shown in Supplementary Figure 2. The reconstruction error depends on the size of the latent dimension Z, i.e., the degree of data compression desired. By testing the performance of autoencoders, we found that the 2D microstructure images with 256 × 256 pixels can be effectively transformed a 16-value representation which can be viewed as a 4 × 4 matrix. The well-trained autoencoders enable the complete encoding and reconstruction of any microstructure frame of the same

type by using only these 16 values in latent space. The pointwise error of 2D images was plotted to visualize the difference between autoencoder-reconstructed 2D images and original ones, and the method for plotting pointwise error has been discussed in Ref.[50].

Machine-learning engine of microstructural evolution

Another key component of this accelerated phase-field framework is the machine learning engine, which learns the dynamics of microstructure evolution within the latent representation space. As history-dependent machine learning techniques, RNN models have been widely adopted as the preferred machine learning engines to accelerate microstructure predictions[45-49]. RNNs are a class of artificial neural networks that use time series data, or sequential data, to predict future data values[67]. In this work, the reduced microstructures of five interdependent phase fields in Ostwald ripening were individually treated as time-series data sets, allowing RNN models to predict their evolution over time. Mathematically, a RNN model consists of a hidden state h and an optional output, both operating on each component, x_t, of the latent vector $\mathbf{x}_t$ within the time sequence $\mathbf{x} = (\mathbf{x}_1, \mathbf{x}_2, ..., \mathbf{x}_N)$. At each time step t, the hidden state h_t of the RNN is updated using a nonlinear activation function f as:

$$h_t = f(h_{t-1}, x_t) \tag{6}$$

where the activation function f can be a simple element-wise sigmoid function in a simple RNN model or a more complex gating function in gate recurrent unit (GRU) and LSTM models. Among these RNN models, LSTM has been proven to be one of the most efficient machine-learned surrogates for phase-field simulations[46,47,49]. Therefore, we primarily use LSTM as the machine learning engine in our accelerated framework for Ostwald ripening.

LSTM learning engine for Ostwald ripening

LSTM was initially introduced as a RNN model used for natural language processing (NLP)[68]. Its architecture typically consists of input, forget, and output gates, as illustrated in Figure 1C. One advantage of LSTM network is that its "memory" can be maintained through the cell state (c_t), which performs continuously throughout the entire LSTM cell. Briefly speaking, the input gate receives a new input point from the microstructure evolution sequence along with the hidden state from the previous time step, determining which values from the input data will be used to modify the cell state. The forget gate decides which parts of the cell state will be forgotten and thus selects the optimal time lag for the input sequence. The output gate combines the processed information and generates the output of the LSTM cell h_t, which is then passed to the next cell h_{t+1} [Figure 1C]. Each gate operates with its own set of weights and biases, allowing the network to effectively capture complex temporal dependencies.

For each field in this Ostwald ripening problem, we train an LSTM model by using the corresponding autoencoder-reduced microstructure sequences in the latent space. We used 80% of the phase-field simulations as the training dataset, while the remaining 20% were reserved for testing. When using LSTM to forecast the future evolution of microstructure in latent space, predicting entire sequences at once would require a very complex and data-intensive model, which exceeds the capability of our available dataset. As such, the LSTM models were trained using a window-shifting method, where a specific window size is specified before training begins. This window size defines the number of time frames the LSTM model will consider as input to predict the next one. For instance, if 80 time frames are selected for training, the window-shifting method uses true time frames 1 through 80 to predict frame 81, which is then stored. Next, true frames 2 through 80 along with the predicted frame 81 are used to predict frame 82.

Since a prior study found that deep LSTM architectures often failed to converge during the training process[46], we used 2 hidden layers and trained each LSTM model for 1,000 epochs for each field. The training and validation loss, as shown in Supplementary Figure 3, indicates that all LSTM models can achieve convergence after around 500 epochs. The mean square error (MSE) loss function was used as the performance metric to assess the training process of LSTM models[69]. All LSTM models were trained and tested using the PyTorch library with Adam optimizer.

Predicting the correlation between coupled phase fields

Support vector machine (SVM) is a supervised learning technique that maps each input to a specific vector in the output space[70]. The output vector is scaled based on the magnitude of the input, and because each input corresponds to a vector with a unique direction, combining these vectors allows the SVM model to reach any point in the output domain. This capability makes SVM particularly effective for capturing the correlation of the microstructure evolution among different fields in latent space.

We trained SVM models to capture the relationships among the autoencoder-reduced representations of the five coupled fields involved in Ostwald ripening. The input to each SVM model is the reduced microstructure sequences of four phases, while the output corresponds to the microstructures of the remaining one field in the latent space. Accordingly, five distinct SVM models were developed for each field in this work. We used 80% of the microstructure sequences for training and the remaining 20% for testing. The performance of the SVM models was evaluated using MSE values as the scoring metric.

RESULTS AND DISCUSSION

Microstructural evolution of Ostwald ripening

Ostwald ripening is a classical phase-field benchmark problem in which multiple phases are coupled with each other and evolve spontaneously[52]. This phenomenon is commonly observed in real material systems, such as the growth and coarsening of γ' precipitates in a γ matrix in nickel-based superalloys[71]. By varying the dominant input parameters (e.g., M, c_a, c_o, and ϵ), a wide range of microstructures can be obtained for the Ostwald ripening problem. Figure 2 illustrates the representative microstructural evolution for both solute and four structural order parameter fields at different time steps. At the initial stage, the conservative c fields (left column in each panel) always consist of small particles, which gradually coalesce into larger particles over time. The four η fields exhibit similar evolutionary behaviors, where the initial small particles merge and grow larger. By comparing the microstructure morphology between the c and the four η fields in Figure 2, it is interesting to see that the η fields consist of particles that are isolated from the c field. Moreover, the sum of all particles in the four η fields is always identical to the c field at all time steps. As time evolves, some isolated particles in the η fields rapidly coalesce and form larger particles, while other small particles may disappear, such as $\eta_{2\text{-}4}$ fields as shown in Figure 2A.

Transforming microstructural evolution in latent space

Based on the diverse microstructural evolution paths of Ostwald ripening, all 2D original images were transformed into the low-dimensional space using autoencoder technique. Mathematically, autoencoder is used to achieve a nonlinear embedding of high-dimensional microstructure data X ($\mathbf{x}$, t) into a low-dimensional representation, Z (x_i, t). Figure 3 shows the autoencoder-reduced features for a representative microstructural evolution of five fields in Ostwald ripening at three different time frames: $t = t_1$, $t = t_{10}$, and $t = t_{100}$. The results demonstrate that the autoencoder effectively transforms the 2D images from 256 × 256 pixels into 4 × 4 reduced matrices for all five fields at different time frames. By using these latent microstructures, the well-trained autoencoder can easily transform them back into the original space, and the agreement with phase-field-simulated images demonstrated the promising performance of autoencoder in reconstructing 2D images for the Ostwald ripening problem Figure 3.

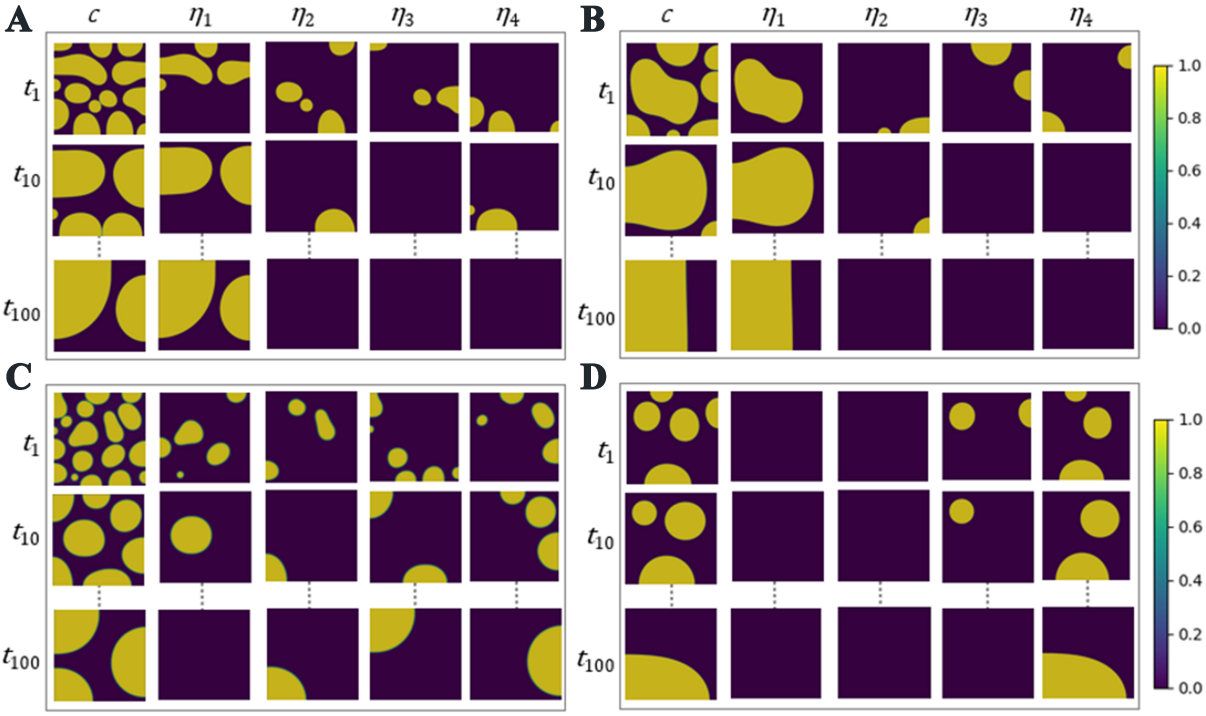

Figure 2. Microstructural evolutions for Ostwald ripening. The screenshots of representative microstructure images of five coupled fields, including one compositional field (c) and four structural order parameters (η_i, i = 1-4) with distinct microstructure features. The input parameters include mobility (M), average initial composition (c_o), and final composition (c_f) for four panels are: (A) M = 4.811, c_o = 0.545, c_f = 0.276; (B) M = 4.864, c_o = 0.500, c_f = 0.279; (C) M = 4.993, c_o = 0.481, c_f = 0.344; (D) M = 4.717, c_o = 0.499, c_f = 0.187.

To further evaluate the performance of autoencoder to capture microstructural evolution in latent space, we plot the first four feature values of the autoencoder-reduced microstructures as a function of total 100 time frames in Figure 3D. As illustrated in the left panel for the c field, these feature values exhibit smooth and continuous variation over time and eventually converge after approximately 80 time frames. This behavior indicates that the autoencoder effectively learns the microstructural evolution of the c field in the reduced space. A similar continuous variation is also observed for the four η fields [Figure 3D], further demonstrating the autoencoder's strong performance in capturing the dynamic evolution of Ostwald ripening with coupled fields in latent space. This finding not only aligns with the manifold hypothesis[60], which suggests that the latent representation of microstructures can effectively mirror its dynamic behaviors over temporal space, but is also consistent with the prior work by Desai *et al.*[61]. That work demonstrated that autoencoders are efficient in representing 2D microstructure images in a relatively smaller dimension, while these reduced features are able to maintain smooth trajectories within this latent space.

It is important to note that the autoencoder-reduced microstructure features do not follow the rule that the sum of four η fields is identical to the c field. This is because the autoencoder is a nonlinear reduction technique, which means it cannot preserve the linear additive relationships of the microstructural features for the five fields in the reduced spaces. Next, we use these reduced features as input parameters for the microstructure-learning engine to accelerate the prediction of evolutionary behavior in Ostwald ripening.

LSTM prediction of microstructure evolution

The LSTM model is chosen as the microstructure-learning engine for Ostwald ripening due to its excellent performance to capture dynamic features of spinodal decomposition in latent space[46,47,49]. Notably, prior

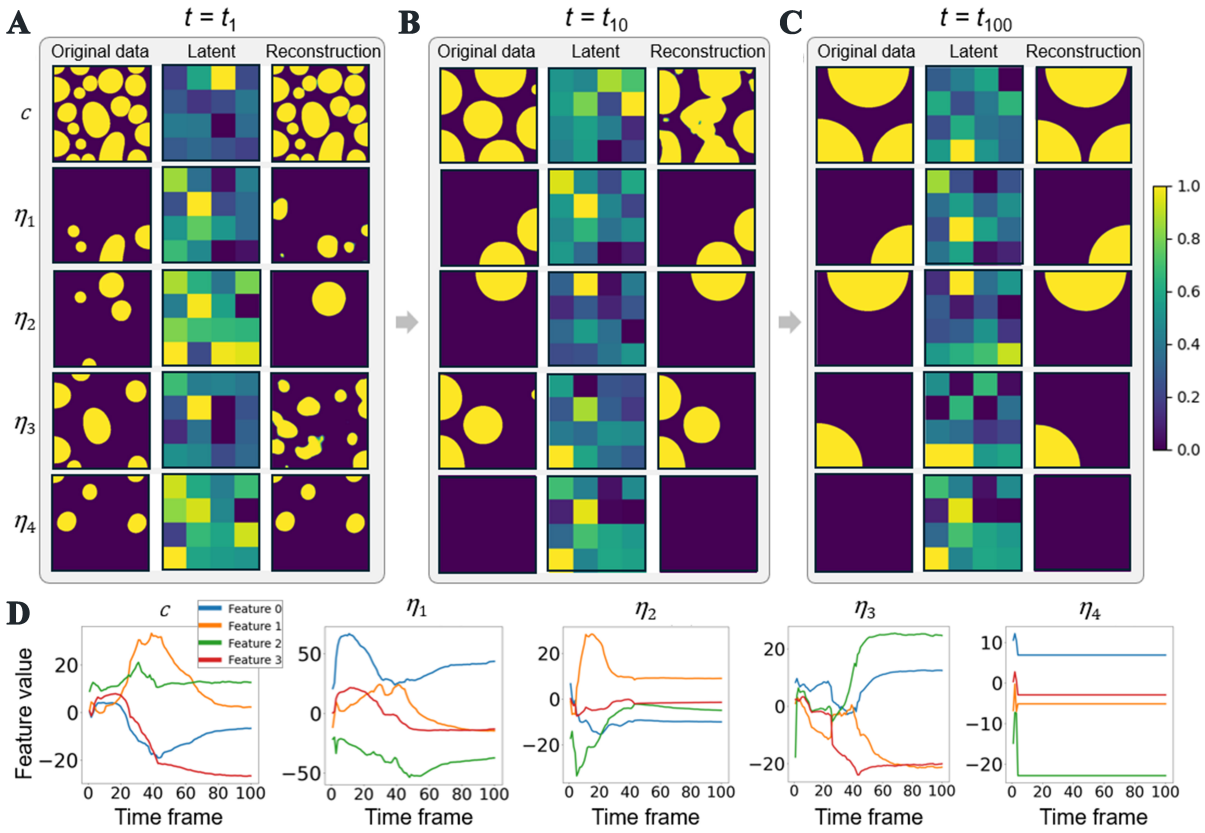

Figure 3. Performance of autoencoder in reducing and reconstructing coupled microstructures. Reduced and reconstructed microstructure of five coupled fields for a representative Oswald ripening simulation at (A) $t = t_1$, (B) $t = t_{10}$, and (C) $t = t_{100}$; (D) Four selected feature values of reduced microstructures are plotted as a function of 100 time frames for each field. The variations of these feature values in the latent space can reflect the real microstructural evolution in the original space based on manifold hypothesis. For instance, the microstructural stability at a certain time frame (e.g., flat curves) in the latent space is equivalent to the stability at that same time frame in the original 2D space. 2D: Two-dimensional.

studies[45,46] have shown that LSTM models achieve best performance in predicting the microstructure of spinodal decomposition when trained on 80 time frames. However, in the case of Ostwald ripening, we found that most of the coupled fields reach a converged state after approximately 75 time frames, with no significant changes thereafter. As a result, training LSTM models with 80 time frames becomes less meaningful for the Ostwald ripening problem. This can be clearly seen in Figure 4A, where the feature values (dotted lines) predicted by the LSTM models trained on 80 frames remain nearly constant from frames 81 to 100 frames, meaning that the microstructures have already converged and no longer evolves during this period. Therefore, our next objective is to identify the optimal training time frames for developing the most efficient LSTM models.

To achieve this, we trained LSTM models using 20, 40, 60, and 80 time frames to study their performance in predicting the latent microstructural features. As shown in Figure 4B, the top four feature values predicted by the LSTM models trained on 60 time frames exhibit perfect agreement with the true feature values from original 2D microstructure images. This suggests that the LSTM models can effectively leverage 60 training frames to predict the future microstructure sequences in Ostwald ripening. When the number of training time frames is reduced to 40, some discrepancies begin to appear between the LSTM-predicted feature values and true values [Figure 4C]. This difference becomes even more pronounced with 20 training time frames [Figure 4D], where the LSTM-predicted feature value curves deviate significantly from the true

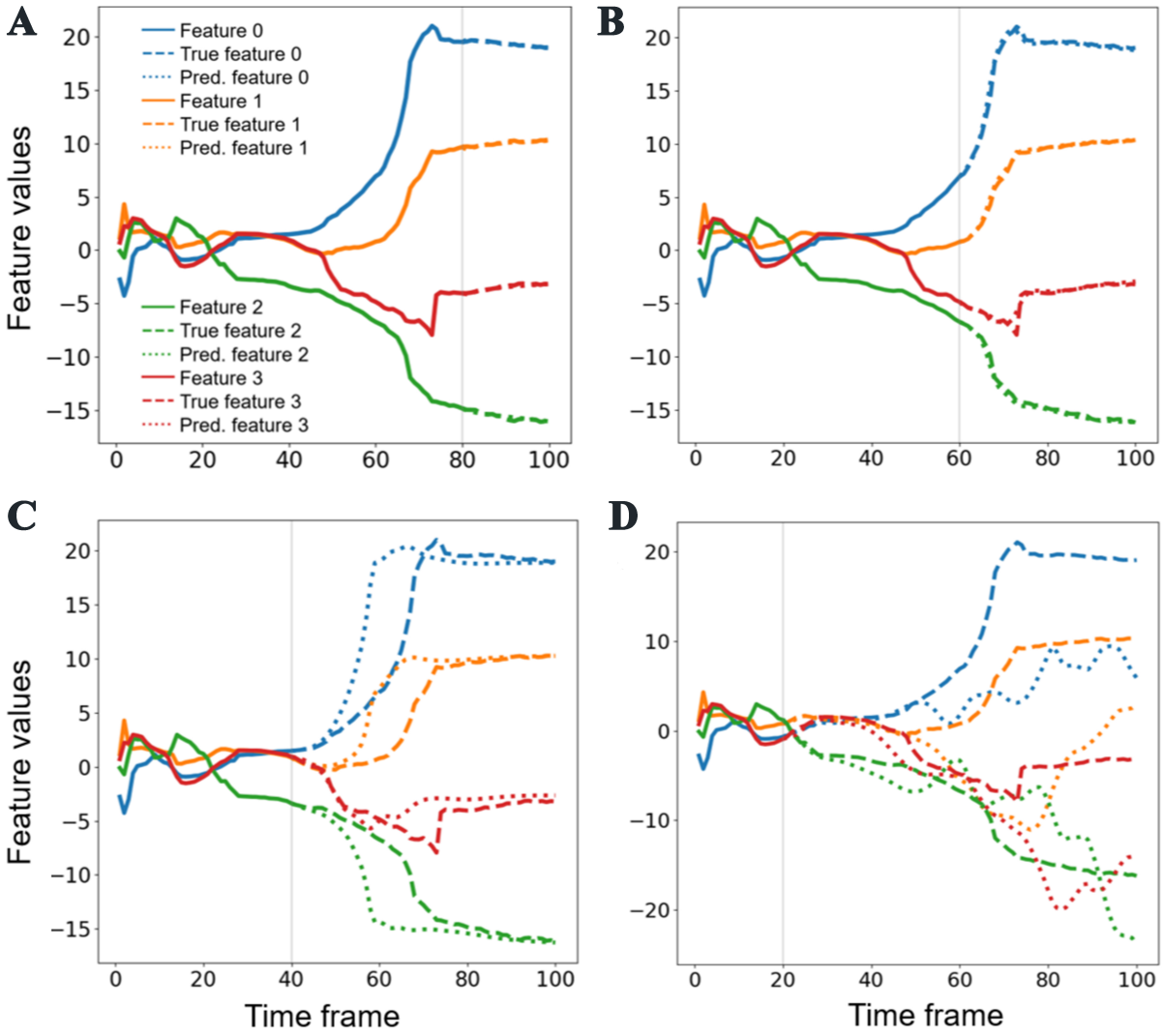

Figure 4. Training performance of LSTM models in predicting the evolution of reduced microstructure with different training time frames. The training loss of LSTM models for predicting the top four autoencoder-reduced microstructural features of compositional field, *c*, using (A) 80 time frames, (B) 60 time frames, (C) 40 time frames, and (D) 20 time frames as the training dataset. The grey dashed lines indicate the starting time frame for LSTM prediction, and the dotted lines after grey dashed lines represent the LSTM-predicted feature values of reduced microstructure evolving as time frames until the last 100 time frame. LSTM: Long short-term memory.

feature values. Based on these observations, we conclude that the optimal training time frames for LSTM models is between 40-60 for Ostwald ripening.

With the optimal time frames, we next evaluate the accuracy of reconstructed microstructure images based on the LSTM-predicted latent representations. To do this, we adopt well-trained autoencoders to decode the latent features back into high-dimensional space and compare the reconstructed images with the original 2D microstructural images. Figure 5 shows a series of reconstructed microstructural images over time for a representative *c* field based on LSTM-predicted latent features using different time frames. When LSTM models are trained with 70 time frames, the reconstructed microstructures using LSTM-reduced features are almost identical to the original 2D images. This similarity is supported by the pointwise error plots in the third row of Figure 5B, which shows that the LSTM-predicted microstructures exhibit small differences

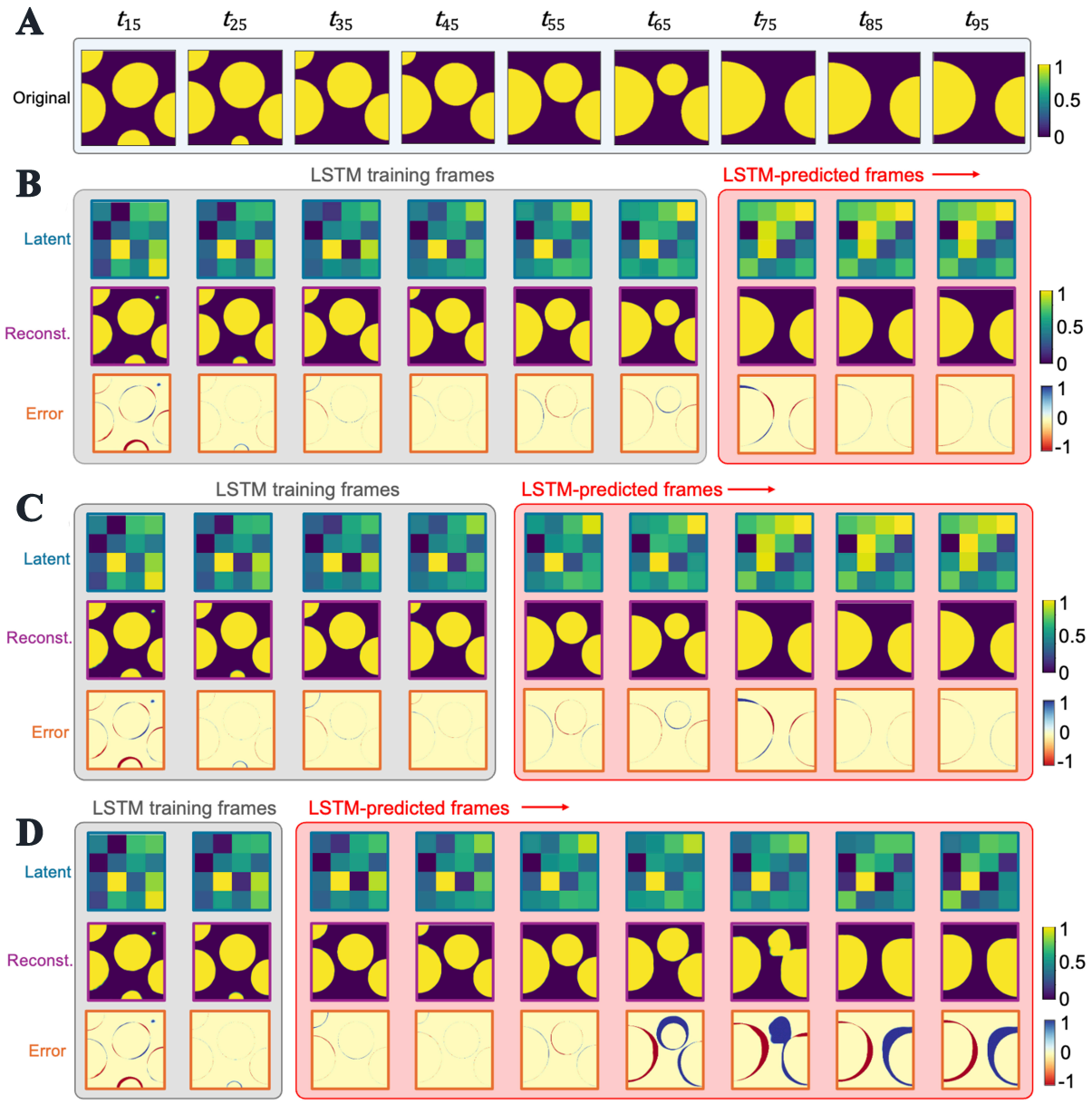

Figure 5. Comparison of microstructural evolution predicted by LSTM models trained with different time frames. The microstructural evolution of composition field *c* in reduced 4 × 4 space and autoencoder-reconstructed 2D space predicted by LSTM models using (B) 70 time frames, (C) 50 time frames, and (D) 30 time frames. The original phase-field-simulated microstructure images at each timestep are shown in panel (A) for comparing the performance of each LSTM model. In panels (B-D), the third rows are pointwise error plots to visualize the differences between the LSTM-predicted microstructure images and original images as a result of the autoencoder (training and predicted frames) and LSTM (predicted frames only). LSTM: Long short-term memory; 2D: two-dimensional.

compared to original one [Figure 5A]. This finding aligns well with our prior analysis, where the LSTM-predicted feature values have perfect agreement with true feature values when time frame is above 60 [Figure 4B]. Moreover, we also adopt LSTM models with 70 training time frames to predict the evolution of four η fields, and the near-perfect match between LSTM-predicted microstructures and true phase-field simulations shown in Supplementary Figure 4 further demonstrates the superior performance of LSTM models in accurately predicting the microstructure evolution of Ostwald ripening problem.

As the training time frames decrease to 50, it becomes more likely for differences to appear between the LSTM-predicted 2D microstructures and the true images [Figure 5C], especially at later time steps such as $t = t_{85}$ and $t = t_{95}$. Furthermore, when using only 30 training time frames, the LSTM-predicted microstructures start to deviate significantly from the true evolution as early as $t = t_{35}$, and frequently diverges completely from the ground-true phase-field simulations [Figure 5D]. This large difference can be clearly seen in the pointwise error plots in Figure 5D. Based on the above microstructural analyses, we can conclude that the optimal training time frames for LSTM models lie between 40 and 60, which is once again consistent with our prior analysis about feature values [Figure 4].

SVM prediction of coupled phase fields in latent space

Although LSTM models demonstrate exceptional performance in predicting the dynamic features of multiple fields, they are not transferable across different fields. More specifically, the LSTM model must be trained separately for each field by using their individual database. These processes significantly limit the efficiency of LSTM models for predicting the microstructural evolution for more complex systems, especially involving a large number of coupled fields. As such, we investigate the correlations between different fields and explore the potential of using machine learning techniques to predict the microstructural evolutions among these coupled fields.

Here, we employ SVM models to predict latent features of one field by using the reduced features of other coupled fields as input parameters. For instance, Figure 6A shows a parity plot of the SVM-predicted latent features of c field by using the other four η fields as the input parameters. The perfect linear correlation between the SVM prediction and actual feature values, along with the low MSE values, suggests the high accuracy and effectiveness of the SVM predictions. Using this SVM model, we can easily predict the reduced microstructure of any c field. For example, the inset of Figure 6A compares the 4 × 4 latent features of a representative c field obtained from the autoencoder with those predicted by the SVM model. The excellent agreement between them further highlights the promising performance of the SVM models in predicting the latent microstructure evolution of the c field.

Similarly, SVM models can be used to predict the latent representation of any of the η fields by using the remaining fields as the input parameters. Figure 6B-E shows the parity plots which compare the SVM prediction with the actual feature values for each η field. The perfect linear correlations observed in these plots further verify the high accuracy of the SVM models in predicting η parameters. By comparing the MSE values, Figure 6 indicates that the c field has a lower MSE value than the four η parameter fields. The lower MSE in the c field is likely due to the non-redundant latent features contributed by the four individual η parameters. In contrast, the latent representation of the c field may already embed information from the reduced η fields, making the SVM predicting of these individual η fields less accurate.

To further assess the performance of SVM in predicting microstructural evolution across different fields, we use well-trained autoencoders to reconstruct the SVM-predicted latent space of each field and compare the results with reconstructed images using the ideal latent features. As shown in Figure 7, the reconstructed microstructures using SVM-predicted microstructure exhibit perfect agreement with actual c and first two η parameter fields (η_1 and η_2). Yet, the prediction performance is less accurate for the microstructures of η_3 and η_4 fields. This can be seen in the relatively large pointwise errors between autoencoder-reconstructed image and original microstructure images in the rightmost column in Figure 7. The slightly lower performance in predicting the η_3 and η_4 fields is indeed due to the autoencoder reconstruction process rather than the SVM prediction, as pointwise error plots shown in the second to last column in Figure 7 compare the reconstruction from the SVM-predicted latent representation to the reconstruction of the original latent

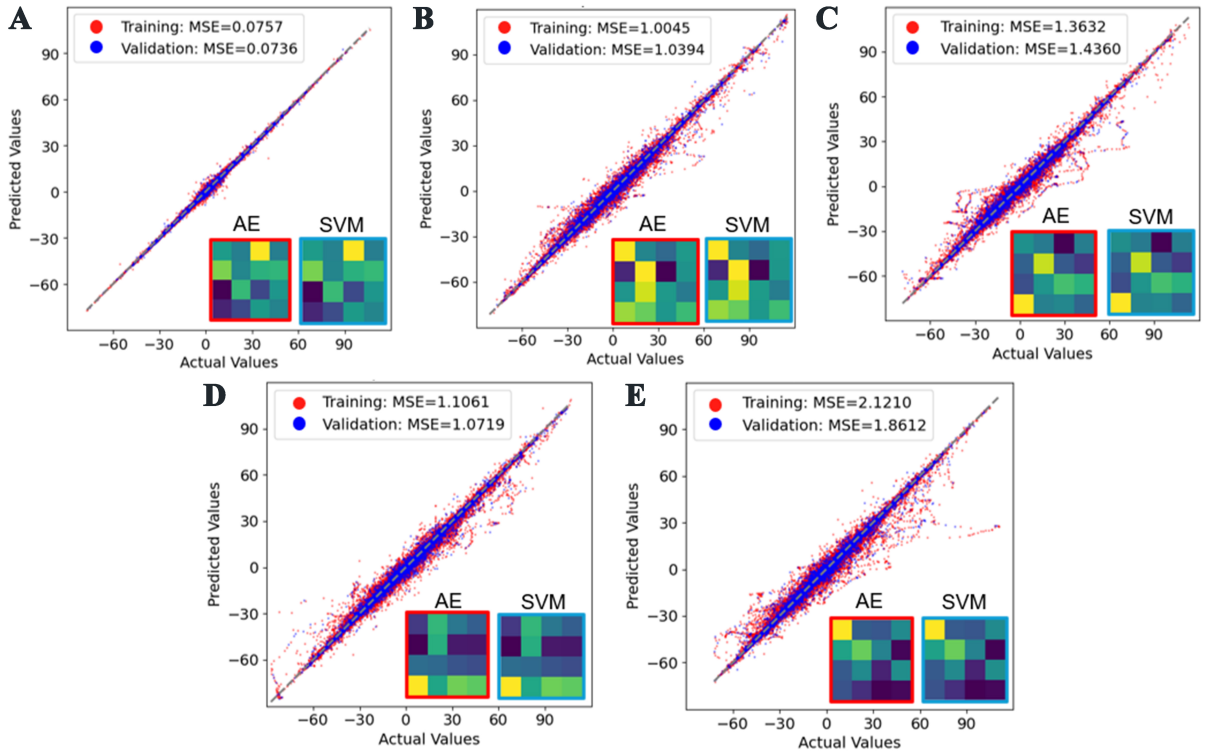

Figure 6. SVM performance in predicting the latent features of five couple fields. Parity plots of SVM-predicted feature values *vs.* AE-reduced feature values of (A) solute compositional field, *c*, and (B-E) four structural order parameter fields, η_i (i = 1-4). The comparison of latent feature values between SVM prediction and AE-reduced values for a representative microstructure of each field is shown as the inset in each panel. SVM: Support vector machine; AE: autoencoder.

representation. This illustrates that for all fields, the SVM exhibits minimal discrepancies beyond the error introduced through the use of the autoencoder.

Despite its promising performance, it is still uncertain whether the SVM is the best method to predict the feature correlation between different phases in this Oswald ripening problem. Here, we selected two additional methods: multilayer perception (MLP) and random forest regression (RFR), to predict the feature correlation between different phases and to compare their performance with that of the SVM model. Supplementary Figure 5 shows the parity plots for predicting the *c* field using three models. It clearly shows that the SVM model exhibits the lowest MSE values among the three, highlighting its superior performance in feature predictions. This also suggests that SVM may be the optimal choice as a machine-learning model for predicting the correlation of latent features between coupled phase-field problems in the future.

Performance of accelerated frameworks for Ostwald ripening

Building on the excellent performance of both LSTM predictions of microstructural evolution in latent space and autoencoder reconstruction process, we next evaluate the overall effectiveness of this accelerated framework in speeding up the phase-field simulations for the Ostwald ripening problem. Table 1 summarizes the LSTM training time (t_{train}), LSTM prediction time ($t_{\text{prediction}}$), and reconstruction time (t_{reconst}) required to transform the reduced microstructure back into 2D space using the autoencoder. Based on these times, we also estimate the computational gain achieved by using LSTM models trained with 20, 40, 60, and 80 time frames. For the optimal time frame 60, the t_{train} is only about 4.8 min to train an accurate LSTM model. Once trained, the $t_{\text{prediction}}$ for using this LSTM model to predict one microstructural evolution in

Table 1. Performance of accelerated phase-field frameworks using different LSTM models

LSTM time frames	t_{train} (min)	$t_{prediction}$ (s)	$t_{reconst}$ (s)	Computational gain
20	4.3	0.046	0.772	3.54×10^5
40	4.8	0.042	0.589	3.44×10^5
60	4.2	0.033	0.400	3.35×10^5
80	2.6	0.018	0.246	2.74×10^5

t_{train} is the time for training one LSTM model. $t_{prediction}$ is the time for predicting the future sequence using LSTM model. $t_{reconst}$ is reconstruction time by using autoencoder to transform latent microstructure back to high-dimensional space. Computational gain is the speed up of using accelerated framework to generate a microstructure image as part of an evolution compared to phase-field simulations. LSTM: Long short-term memory.

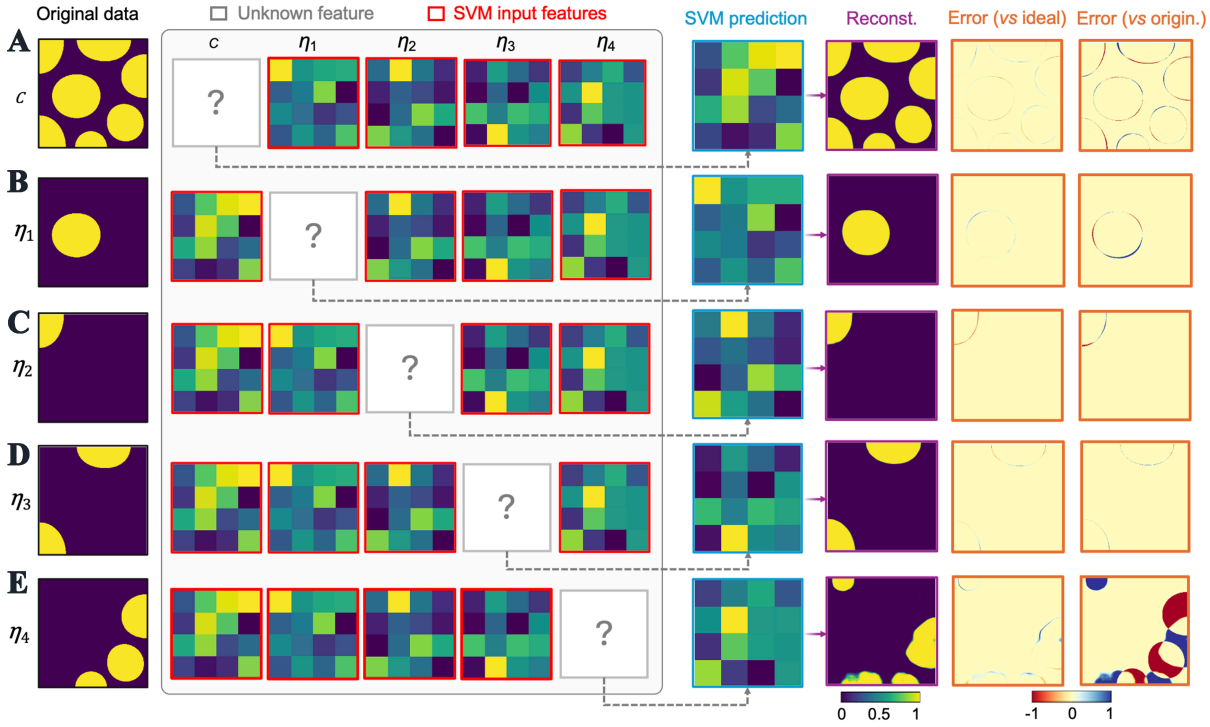

Figure 7. Comparison of reconstructed microstructure using SVM-predicted latent features and autoencoder-reduced features. The original microstructure, SVM input parameters for predicting latent microstructural features, reconstructed microstructure prediction, pointwise error plots between reconstructed microstructures of SVM-predicted features and autoencoder-reduced features (ideal), and pointwise error plots between SVM-predicted features and original images for (A) compositional field, c, and (B-E) four structural order parameter fields, η_i (i = 1-4). SVM: Support vector machine.

latent space over the last 40 time steps takes only 0.033 s. Meanwhile, the $t_{reconst}$ required to transform these reduced images back into high-dimensional 2D images is approximately 0.772 s. Overall, the total time required to predict the microstructural evolution in the original 2D space is about 0.818 s. As such, our accelerated framework achieves a computational speedup of 3.35×10^5 compared to high-fidelity phase field simulations [Table 1].

By comparing with the accelerated framework using an LSTM model with 40 training time frames, t_{train}, $t_{prediction}$, and $t_{reconst}$ are all slightly longer than the 60 training time frames. This is expected, as the LSTM models trained on 40 time frames will need to predict the microstructual evolution of the remaining 60 time frames, increasing the overal computational load. Although the corresponding computational gain (3.44 ×

10^5) is slightly higher than that achieved with 60 training frames, it comes at the cost of reduced predicting accuracy for microstructure evolution in latent space. Thus, we estimate the optimal computational gain of our accelerated framework to be approximately 3.35×10^5 for Ostwald ripening, which represents a significant speedup compared to high-fidelity phase-field simulations.

Furthermore, integrating SVM models into our accelerated phase-field framework improves the overall efficiency. For instance, once the framework is established for any four fields, SVM models can be employed to predict the latent dynamic features of the remaining field. Subsequently, these predicted latent representations can be reconstructed into the original 2D microstructure using the well-trained autoencoder. In this way, there is no need to develop an LSTM model for the remaining field, thereby significantly improving the overall computational efficiency of the accelerated phase-field framework.

Limitations and future work

The accelerated framework demonstrates the feasibility of expediting the phase-field simulations for coupled microstructural evolution. Through the analysis of microstructure prediction performance, we found that autoencoder-based LSTM models exhibit high accuracy and efficiency in forecasting the microstructure evolution within the latent space. However, there are several limitations of this accelerated framework that should be acknowledged. First, as shown in Figure 7, the autoencoder sometimes has trouble recreating the 2D microstructures of the η fields from the latent space. This limitation is likely due to the relatively simple microstructure patterns presented in the η fields compared to the c field, as well as the limited size of microstructure database (200 simulations), which may be insufficient for training a robust autoencoder-based neural network. The second limitation is that LSTM models are heavily dependent on the number of time frames used for their training, as these models demonstrate lower performance when trained with a smaller number of time steps [Figure 4]. Thus, enhancing the predictive performance of LSTM models with fewer number of time frames is crucial for improving the overall efficiency of the accelerated phase-field framework.

It is worthy to note that an interesting direction for accelerating Ostwald ripening is the development of physics-informed models, such as PSDMs based on U-Net[51]. This approach is motivated by recent studies which demonstrate that the PSDMs can achieve very high accuracy in predicting the microstructural evolution with low prediction error and reduced error accumulation during autoregressive predictions[39]. According to a review article by Dingreville *et al.*, the accelerated framework developed for Ostwald ripening falls in the category of LDM formulation, as the microstructure evolution is predicted within the latent space[39]. Since LDMs typically scale better with smaller dataset[39], we anticipate the accelerated framework will outperform the PSDMs in modeling Owstwald ripening. Yet, as the size of database increased or microstructural features become more complex, PSDMs are expected to outperform LDMs in predictive performance for coupled microstructure evolution.

Although the accelerated framework developed in this study is for 2D Ostwald ripening problem, it is anticipated that this framework can be easily extended to the 3D systems. This is because the microstructural features in both 2D and 3D cases always share similar evolutionary behaviors, which indicates that the key features in latent space demonstrate similar variations, making it easier for machine-learning models to capture them. Additionally, our accelerated framework is applicable to the more complex, coupled phase-field problems by incorporating various physical coupling interactions between various fields, such as elastic strain, component diffusion heterogeneity, and inhomogeneous interface energy. Once the new microstructural database is developed, the accelerated framework can be readily retrained to capture the new microstructural features in latent representations and predict their evolution

over time sequences. This also indicates the high potential of this accelerated phase-field framework for adapting to new phase-field problems.

CONCLUSIONS

In this work, we developed an accelerated phase-field framework for Ostwald ripening problems. This framework integrates the high-throughput phase-field simulations for generating large datasets of 2D microstructure images, autoencoder-based image reduction techniques, and LSTM models as machine-learning engine for predicting the microstructural evolutions in latent space. A high-quality database of microstructure evolution containing 200 Ostwald ripening trajectories was developed. Based on this large database, we found that the autoencoder can efficiently capture the key features of Ostwald ripening microstructure images in the low-dimensional dimensions for five different fields: including one solute compositional field and four structural order parameter fields. The reduced microstructures were subsequently fed into the LSTM models to predict the evolution of microstructures for all five fields. These models do not only exhibit high performance in accurately predicting the dynamics of coupled microstructures, but also achieve a significant speedup of 3.35×10^5 compared to high-fidelity phase-field simulations. Additionally, the SVM models were implemented to successfully predict the correlation between the difference fields, further improving the computational efficiency of our accelerated framework. The accelerated frameworks developed in this study are not only applicable to the 2D Ostwald ripening problems, but also have the potential to predict microstructural evolution in more complex systems involving multiple coupled fields in 3D space. As the datasets for microstructure evolutions continue to grow, the framework developed in this work may become less efficient. Therefore, the development of physics-informed PSDMs could represent a potentially future research direction for accelerating coupled phase-field problems.

DECLARATIONS

Acknowledgments

The authors thank Dr. Remi Dingreville and Dr. Daniel Vizoso for valuable discussions regarding the use of the MEMPHIS code.

Authors' contributions

Data curation (lead); formal analysis (lead); investigation (lead); methodology (lead); visualization (lead); writing - original draft (lead); writing - review and editing (lead): Gesch, A.

Conceptualization; supervision; formal analysis (lead); investigation (lead); methodology (lead); visualization (lead); writing - original draft (lead); writing - review and editing (lead): Hu, C.

Availability of data and materials

The data and codes are available on publicly accessible platforms. All microstructure databases can be accessed through the MDF website using following link[59]. The machine-learning codes developed for the accelerated framework are available on GitHub website: https://github.com/huhuhhhh/AcceleratePF.

Financial support and sponsorship

This work was supported by the University of Alabama startup fund. Computational resources were provided by the Alabama Supercomputer Authority (ASA). This work was partially conducted using the resources at the National Energy Research Scientific Computing Center, a DOE Office of Science User Facility supported by the Office of Science of the U.S. Department of Energy under Contract No. DE-AC02-05CH11231 using NERSC award BES-ERCAP0031213.

Conflicts of interest

Both authors declared that there are no conflicts of interest.

Ethical approval and consent to participate

Not applicable.

Consent for publication

Not applicable.

Copyright

REFERENCES

1. Chen, L. Q. Phase-field models for microstructure evolution. *Annu. Rev. Mater. Res.* **2002**, *32*, 113-40. DOI
2. Boettinger, W. J.; Warren, J. A.; Beckermann, C.; Karma, A. Phase-field simulation of solidification. *Annu. Rev. Mater. Res.* **2002**, *32*, 163-94. DOI
3. Steinbach, I. Phase-field models in materials science. *Modelling. Simul. Mater. Sci. Eng.* **2009**, *17*, 073001. DOI
4. Moelans, N.; Blanpain, B.; Wollants, P. An introduction to phase-field modeling of microstructure evolution. *Calphad* **2008**, *32*, 268-94. DOI
5. Cahn, J. W. On spinodal decomposition. *Acta. Metall.* **1961**, *9*, 795-801. DOI
6. Su, Y.; Liang, C.; Wang, D. Composition- and temperature-dependence of β to ω phase transformation in Ti-Nb alloys. *J. Mater. Inf.* **2023**, *3*, 14. DOI
7. Voorhees, P. W. The theory of Ostwald ripening. *J. Stat. Phys.* **1985**, *38*, 231-52. DOI
8. Krill III, C. E.; Chen, L. Q. Computer simulation of 3-D grain growth using a phase-field model. *Acta. Mater.* **2002**, *50*, 3059-75. DOI
9. Moelans, N.; Wendler, F.; Nestler, B. Comparative study of two phase-field models for grain growth. *Comput. Mater. Sci.* **2009**, *46*, 479-90. DOI
10. Moelans, N.; Blanpain, B.; Wollants, P. Quantitative analysis of grain boundary properties in a generalized phase field model for grain growth in anisotropic systems. *Phys. Rev. B.* **2008**, *78*, 024113. DOI
11. Karma, A.; Rappel, W. Quantitative phase-field modeling of dendritic growth in two and three dimensions. *Phys. Rev. E.* **1998**, *57*, 4323-49. DOI
12. Warren, J.; Boettinger, W. Prediction of dendritic growth and microsegregation patterns in a binary alloy using the phase-field method. *Acta. Metall. Mater.* **1995**, *43*, 689-703. DOI
13. Takaki, T. Phase-field modeling and simulations of dendrite growth. *ISIJ. Int.* **2014**, *54*, 437-44. DOI
14. Stefanovic, P.; Haataja, M.; Provatas, N. Phase-field crystals with elastic interactions. *Phys. Rev. Lett.* **2006**, *96*, 225504. DOI PubMed
15. Boussinot, G.; Le Bouar, Y.; Finel, A. Phase-field simulations with inhomogeneous elasticity: comparison with an atomic-scale method and application to superalloys. *Acta. Mater.* **2010**, *58*, 4170-81. DOI
16. Shchyglo, O.; Ali, M. A.; Salama, H. Efficient finite strain elasticity solver for phase-field simulations. *npj. Comput. Mater.* **2024**, *10*, 1235. DOI
17. Kim, J. Phase field computations for ternary fluid flows. *Comput. Methods. Appl. Mech. Eng.* **2007**, *196*, 4779-88. DOI
18. Jeong, J. H.; Goldenfeld, N.; Dantzig, J. A. Phase field model for three-dimensional dendritic growth with fluid flow. *Phys. Rev. E.* **2001**, *64*, 041602. DOI PubMed
19. Celani, A.; Mazzino, A.; Muratore-Ginanneschi, P.; Vozella, L. Phase-field model for the Rayleigh–Taylor instability of immiscible fluids. *J. Fluid. Mech.* **2009**, *622*, 115-34. DOI
20. Wu, J. Y.; Nguyen, V. P.; Nguyen, C. T.; Sutula, D.; Sinaie, S.; Bordas, S. P. A. Chapter One - Phase-field modeling of fracture. *Adv. Appl. Mech.* **2020**, *53*, 1-183. DOI
21. Miehe, C.; Schänzel, L.; Ulmer, H. Phase field modeling of fracture in multi-physics problems. Part I. Balance of crack surface and failure criteria for brittle crack propagation in thermo-elastic solids. *Comput. Methods. Appl. Mech. Eng.* **2015**, *294*, 449-85. DOI
22. Miehe, C.; Hofacker, M.; Schänzel, L.; Aldakheel, F. Phase field modeling of fracture in multi-physics problems. Part II. Coupled brittle-to-ductile failure criteria and crack propagation in thermo-elastic–plastic solids. *Comput. Methods. Appl. Mech. Eng.* **2015**, *294*, 486-522. DOI
23. Dutil, Y.; Rousse, D. R.; Salah, N. B.; Lassue, S.; Zalewski, L. A review on phase-change materials: mathematical modeling and simulations. *Renew. Sustain. Energy. Rev.* **2011**, *15*, 112-30. DOI
24. Bui, T. Q.; Hu, X. A review of phase-field models, fundamentals and their applications to composite laminates. *Eng. Fract. Mech.* **2021**, *248*, 107705. DOI
25. Raina, A.; Miehe, C. A phase-field model for fracture in biological tissues. *Biomech. Model. Mechanobiol.* **2016**, *15*, 479-96. DOI

PubMed

26. Tonks, M. R.; Gaston, D.; Millett, P. C.; Andrs, D.; Talbot, P. An object-oriented finite element framework for multiphysics phase field simulations. *Comput. Mater. Sci.* **2012**, *51*, 20-9. DOI
27. Gültekin, O.; Dal, H.; Holzapfel, G. A. A phase-field approach to model fracture of arterial walls: theory and finite element analysis. *Comput. Methods. Appl. Mech. Eng.* **2016**, *312*, 542-66. DOI PubMed PMC
28. Yue, P.; Zhou, C.; Feng, J. J.; Ollivier-Gooch, C. F.; Hu, H. H. Phase-field simulations of interfacial dynamics in viscoelastic fluids using finite elements with adaptive meshing. *J. Comput. Phys.* **2006**, *219*, 47-67. DOI
29. Wang, C.; Wise, S. M. An energy-stable and convergent finite-difference scheme for the modified phase field crystal equation. *SIAM. J. Numer. Anal.* **2011**, *49*, 945-69. DOI
30. Hu, Z.; Wise, S. M.; Wang, C.; Lowengrub, J. S. Stable and efficient finite-difference nonlinear-multigrid schemes for the phase field crystal equation. *J. Comput. Phys.* **2009**, *228*, 5323-39. DOI
31. Liu, H.; Valocchi, A. J.; Zhang, Y.; Kang, Q. Phase-field-based lattice Boltzmann finite-difference model for simulating thermocapillary flows. *Phys. Rev. E.* **2013**, *87*, 013010. DOI
32. Gain, A. L.; Paulino, G. H. Phase-field based topology optimization with polygonal elements: a finite volume approach for the evolution equation. *Struct. Multidisc. Optim.* **2012**, *46*, 327-42. DOI
33. Chen, L. Q.; Shen, J. Applications of semi-implicit Fourier-spectral method to phase field equations. *Comput. Phys. Commun.* **1998**, *108*, 147-58. DOI
34. Liu, C.; Shen, J. A phase field model for the mixture of two incompressible fluids and its approximation by a Fourier-spectral method. *Physica. D.* **2003**, *179*, 211-28. DOI
35. Feng, W. M.; Yu, P.; Hu, S. Y.; Liu, Z. K.; Du, Q.; Chen, L. Q. Spectral implementation of an adaptive moving mesh method for phase-field equations. *J. Comput. Phys.* **2006**, *220*, 498-510. DOI
36. Shen, J.; Yang, X. An efficient moving mesh spectral method for the phase-field model of two-phase flows. *J. Computat. Phys.* **2009**, *228*, 2978-92. DOI
37. Muranushi, T. Paraiso: an automated tuning framework for explicit solvers of partial differential equations. *Comput. Sci. Disc.* **2012**, *5*, 015003. DOI
38. Yamanaka, A.; Aoki, T.; Ogawa, S.; Takaki, T. GPU-accelerated phase-field simulation of dendritic solidification in a binary alloy. *J. Cryst. Growth.* **2011**, *318*, 40-5. DOI
39. Dingreville, R.; Roberston, A. E.; Attari, V.; et al. Benchmarking machine learning strategies for phase-field problems. *Modelling. Simul. Mater. Sci. Eng.* **2024**, *32*, 065019. DOI
40. Teichert, G. H.; Garikipati, K. Machine learning materials physics: surrogate optimization and multi-fidelity algorithms predict precipitate morphology in an alternative to phase field dynamics. *Comput. Methods. Appl. Mech. Eng.* **2019**, *344*, 666-93. DOI
41. Teichert, G.; Natarajan, A.; Van der Ven, A.; Garikipati, K. Machine learning materials physics: integrable deep neural networks enable scale bridging by learning free energy functions. *Comput. Methods. Appl. Mech. Eng.* **2019**, *353*, 201-16. DOI
42. Wang, Z.; Huan, X.; Garikipati, K. Variational system identification of the partial differential equations governing the physics of pattern-formation: inference under varying fidelity and noise. *Comput. Methods. Appl. Mech. Eng.* **2019**, *356*, 44-74. DOI
43. Yabansu, Y. C.; Steinmetz, P.; Hötzer, J.; Kalidindi, S. R.; Nestler, B. Extraction of reduced-order process-structure linkages from phase-field simulations. *Acta. Mater.* **2017**, *124*, 182-94. DOI
44. Herman, E.; Stewart, J. A.; Dingreville, R. A data-driven surrogate model to rapidly predict microstructure morphology during physical vapor deposition. *Appl. Math. Model.* **2020**, *88*, 589-603. DOI
45. Montes de Oca Zapiain, D.; Stewart, J. A.; Dingreville, R. Accelerating phase-field-based microstructure evolution predictions via surrogate models trained by machine learning methods. *npj. Comput. Mater.* **2021**, *7*, 471. DOI
46. Hu, C.; Martin, S.; Dingreville, R. Accelerating phase-field predictions via recurrent neural networks learning the microstructure evolution in latent space. *Comput. Methods. Appl. Mech. Eng.* **2022**, *397*, 115128. DOI
47. Fetni, S.; Pham, T. Q. D.; Hoang, T. V.; et al. Capabilities of auto-encoders and principal component analysis of the reduction of microstructural images; application on the acceleration of phase-field simulations. *Comput. Mater. Sci.* **2023**, *216*, 111820. DOI
48. Wu, P.; Iquebal, A. S.; Ankit, K. Emulating microstructural evolution during spinodal decomposition using a tensor decomposed convolutional and recurrent neural network. *Comput. Mater. Sci.* **2023**, *224*, 112187. DOI
49. Ahmad, O.; Kumar, N.; Mukherjee, R.; Bhowmick, S. Accelerating microstructure modeling via machine learning: a method combining Autoencoder and ConvLSTM. *Phys. Rev. Mater.* **2023**, *7*, 083802. DOI
50. Zhou, X.; Sun, S.; Cai, S.; et al. Accelerating three-dimensional phase-field simulations via deep learning approaches. *J. Mater. Sci.* **2024**, *59*, 15727-37. DOI
51. Oommen, V.; Shukla, K.; Desai, S.; Dingreville, R.; Karniadakis, G. E. Rethinking materials simulations: blending direct numerical simulations with neural operators. *npj. Comput. Mater.* **2024**, *10*, 1319. DOI
52. Jokisaari, A.; Voorhees, P.; Guyer, J.; Warren, J.; Heinonen, O. Benchmark problems for numerical implementations of phase field models. *Comput. Mater. Sci.* **2017**, *126*, 139-51. DOI
53. Balluffi, R. W.; Allen, S. M.; Carter, W. C. Kinetics of materials. John Wiley & Sons; 2005. DOI
54. Allen, S. M.; Cahn, J. W. A microscopic theory for antiphase boundary motion and its application to antiphase domain coarsening. *Acta. Metall.* **1979**, *27*, 1085-95. DOI
55. Stewart, J. A.; Dingreville, R. Microstructure morphology and concentration modulation of nanocomposite thin-films during simulated

physical vapor deposition. *Acta. Mater.* **2020**, *188*, 181-91. DOI

56. Monti, J. M.; Hopkins, E. M.; Hattar, K.; Abdeljawad, F.; Boyce, B. L.; Dingreville, R. Stability of immiscible nanocrystalline alloys in compositional and thermal fields. *Acta. Mater.* **2022**, *226*, 117620. DOI
57. Blaiszik, B.; Chard, K.; Pruyne, J.; Ananthakrishnan, R.; Tuecke, S.; Foster, I. The materials data facility: data services to advance materials science research. *JOM.* **2016**, *68*, 2045-52. DOI
58. Blaiszik, B.; Ward, L.; Schwarting, M.; et al. A data ecosystem to support machine learning in materials science. *MRS. Commun.* **2019**, *9*, 1125-33. DOI
59. Gesch, A. H.; Hu, C. Ostwald Ripening Dataset for "Accelerating phase-field simulation of coupled microstructural evolution using autoencoder-based recurrent neural networks". 2025. DOI
60. Cho, K.; van, M. B.; Gulcehre, C.; et al. Learning phrase representations using RNN encoder-decoder for statistical machine translation. *arXiv* **2014**, arXiv:1406.1078. https://doi.org/10.48550/arXiv.1406.1078. (accessed 9 Jun 2025)
61. Desai, S.; Shrivastava, A.; D'elia, M.; Najm, H. N.; Dingreville, R. Trade-offs in the latent representation of microstructure evolution. *Acta. Mater.* **2024**, *263*, 119514. DOI
62. Bank, D.; Koenigstein, N.; Giryes, R. Autoencoders. In: Rokach L, Maimon O, Shmueli E, editors. Machine Learning For Data Science Handbook. Cham: Springer International Publishing; 2023. pp. 353-74. DOI
63. Hu, A.; Liu, Z.; Chen, Q.; et al. A new framework for predicting tensile stress of natural rubber based on data augmentation and molecular dynamics simulation data. *J. Mater. Inf.* **2024**, *4*, 11. DOI
64. Chowdhury, A.; Kautz, E.; Yener, B.; Lewis, D. Image driven machine learning methods for microstructure recognition. *Comput. Mater. Sci.* **2016**, *123*, 176-87. DOI
65. Chan, H.; Cherukara, M.; Loeffler, T. D.; Narayanan, B.; Sankaranarayanan, S. K. R. S. Machine learning enabled autonomous microstructural characterization in 3D samples. *npj. Comput. Mater.* **2020**, *6*, 267. DOI
66. Creswell, A.; Arulkumaran, K.; Bharath, A. A. On denoising autoencoders trained to minimise binary cross-entropy. *arXiv* **2017**, arXiv:1708.08487. https://doi.org/10.48550/arXiv.1708.08487. (accessed 9 Jun 2025)
67. Tealab, A. Time series forecasting using artificial neural networks methodologies: a systematic review. *Future. Comput. Informatics. J.* **2018**, *3*, 334-40. DOI
68. Hochreiter, S.; Schmidhuber, J. Long short-term memory. *Neural. Comput.* **1997**, *9*, 1735-80. DOI PubMed
69. Naser, M. Z.; Alavi, A. H. Error metrics and performance fitness indicators for artificial intelligence and machine learning in engineering and sciences. *Archit. Struct. Constr.* **2023**, *3*, 499-517. DOI
70. Cortes, C.; Vapnik, V. Support-vector networks. *Mach. Learn.* **1995**, *20*, 273-97. DOI
71. Zhu, J. Z.; Wang, T.; Ardell, A. J.; Zhou, S. H.; Liu, Z. K.; Chen, L. Q. Three-dimensional phase-field simulations of coarsening kinetics of γ′ particles in binary Ni–Al alloys. *Acta. Mater.* **2004**, *52*, 2837-45. DOI